# Hypothesis Validation of Far Wall Brightness in Carotid Artery Ultrasound for Feature-Based IMT Measurement using a Combination of Level Set Segmentation & Registration

Filippo Molinari, Ganapathy Krishnamurthi, U. Rajendra Acharya, S. Vinitha Sree, Guang Zeng, Luca Saba, Andrew Nicolaides, Jasjit S. Suri, *Fellow AIMBE*

***Abstract*—Intima Media Thickness (IMT) is now being considered as an indicator of atherosclerosis. Our group has developed several feature-based IMT measurement algorithms such as CALEX (a class of patented AtheroEdge™ Systems from Global Biomedical Technologies, Inc., CA, USA). These methods are based on the hypothesis that the highest pixel intensities are in the far wall of the Common Carotid Artery (CCA) or the Internal Carotid Artery (ICA). In this work, we verify that this hypothesis holds true for B-mode longitudinal ultrasound images of the carotid wall. This patented methodology consists of generating the composite image (arithmetic sum of images) from the database by first registering the carotid image frames with respect to a nearly straight carotid artery frame from the same database using (a) B-spline based non-rigid registration and (b) affine registration. Prior to registration, we segment the carotid artery lumen using a level set based algorithm followed by morphological image processing. The binary lumen images are registered and the transformations are applied to the original grayscale CCA images. We evaluated our technique using a database of 200 common carotid images of normal and pathologic carotids. The composite image presented the highest intensity distribution in the far wall of the CCA/ICA, validating our hypothesis. We have also demonstrated the accuracy and improvement in IMT segmentation result with our CALEX 3.0 system. The CALEX system, when run on newly acquired ultrasound images, shows the IMT error of about 30 µm. Thus, we have shown that the CALEX algorithm is able to exploit the far wall brightness for accurate IMT measurements.**

***Index Terms*: Carotid Artery, Ultrasound, Far Wall, Brightness, Intima Media Thickness, non-rigid registration, level set segmentation, Performance.**

## I. Introduction

Manuscript received June 22, 2011.

Filippo Molinari is with Biolab, Department of Electronics, Politecnico di Torino, Torino, Italy (email: filippo.molinari@polito.it).

Ganapathy Krishnamurthi and Guang Zeng are with Mayo Clinic, Rochester, MN, USA (e-mail:ganapathy.krishnamurthi@gmail.com; gzen@clemson.edu )

Rajendra Acharya is with Ngee Ann polytechnic, department of Biomedical engineering, Singapore (e-mail: aru@np.edu.sg)

S Vinitha Sree is affiliated with Global Biomedical Technologies Inc., CA, USA (email: vinitha.sree@gmail.com)

Luca Saba is with Department of Science of the Images, Policlinico Universitario, s.s. 554 Monserrato, Cagliari 09045, Italy (email: lucasaba@tiscali.it)

Andrew Nicolaides is with Imperial college, London, UK (email:a.nicolaides@imperial.ac.uk)

Jasjit S. Suri is a CTO with Global Biomedical Technologies, CA, USA and is also affiliated with Biomedical Engineering Department, Idaho State University, ID, USA (email:jsuri@comcast.net).

Atherosclerosis is the thickening and narrowing of the arteries due to formation of plaque on the walls of the artery. It is one of the leading causes of stroke and is the first clinical manifestation of cardiovascular disease. Recent research has been focused on determining early indicators of atherosclerosis. IMT is an early indicator of atherosclerosis [1] and precedes luminal narrowing due to plaque formation. Since plaque formation starts in the walls of the artery, IMT could be a better indicator than lumen area or blood velocity. Population studies have shown a strong correlation between carotid IMT and several cardiovascular risk factors [2] and IMT has also been found to be associated with the extent of atherosclerosis and end organ damage of high-risk patients [3]. B-mode ultrasound (US) is a non-invasive method to measure IMT especially in easily accessible arteries like the carotid. IMT measurements using ultrasonography correlate well with histopathology and are reproducible [4].

Automated segmentation facilitates real time IMT measurements and is very helpful in the clinical evaluation of large databases which can be done either semi-automatically or by running automated methods (so-called batch mode processing). These methods can be applied to several blood vessels. However, several groups such as Liguori *et al*. [5], Cheng *et al*. [6], and Gutierrez *et al.* [7] have proposed methods that require the user to interactively place markers or draw regions of interest to initiate the segmentation. None of these methods are fully automated, and therefore, we seek to define an approach that would require no user interaction.

Our patented system CALEX (Completely Automated Layers EXtraction) (a Class of AtheroEdge™ systems) [8] quantifies IMT using a feature-based approach and is fully automated with minimal user intervention. This system extracts features from the far wall based on the hypothesis that the far wall is brighter [8] compared to the near wall in the US image. Delsanto *et al.* [9] characterized the performance of an automated carotid wall segmentation algorithm based on the same hypothesis by validating against expert segmentation. The algorithm localized the adventitial wall based on the intensity local maxima of every column in the image, *i.e.,* the far wall brightness compared to the near wall. Several systems developed by our group that were based on this hypothesis for IMT measurements produced results that were in good agreement with expert segmentation [8-10]. However, the validation was based on manual intensity measurements on

several representative US images.

In this paper, we validate the hypothesis of far wall maximum brightness by registering our entire database of 200 US images of the carotid artery and showing that the far wall has higher intensity. In addition, we also look at the feasibility of automatic lumen segmentation and registration of B-mode US carotid artery images for clinical studies. Here, we are registering images to a 'standard carotid artery' but we can adapt the same method for images obtained during follow up studies involving the same patient. After registration, we segment the images using an automated technique, in order to show the performance and exploit the potentialities of the registered images. The concept of joint registration and segmentation in one system is not new and it has been adapted before to mammographic images by Suri *et al.* [11]. In fact, it has been shown that registration can improve segmentation performance and vice-versa thereby improving the overall quality of the examination [11].

The paper is organized as follows. Section II talks about image acquisition and pre-processing steps and also describes the segmentation and registration methods. In Section III, we present the results obtained using registration and segmentation. A detailed discussion is presented in Section IV. In Section V, we look at how we can exploit the higher intensity of the far wall for automatic carotid artery segmentation. We conclude the paper in Section VI.

## II. METHODS

### A. Image acquisition and normalization

The image database consists of 200 B-mode 2D US longitudinal images of the common tract of the carotid artery. All the images were transferred to a computer via a DICOM communication port in log-compressed 8-bit grayscale. The pixel density of all the images was equal to 16 pixels/mm in the axial direction, thus leading to a conversion factor of 0.0625 mm/pixel. The images were taken from 130 subjects: 50 normal subjects and 80 patients suffering from atherosclerosis who were recruited by the Neurology division of the Gradenigo Hospital (Torino, Italy) where all the US examinations were conducted. 100 images were relative to the left and right carotid artery of the 50 healthy subjects. 160 images were acquired from the 80 patients, one each from the left and right carotid arteries. However, among these 160 images, we had to discard 60 images: 35 carotids had a plaque protruding in the artery lumen, whereas 25 images were relative to pre-treated carotids (*i.e.*, the carotid was either closed or with an implanted stent). These 60 images were unsuitable to test our hypothesis, because our methodology has not been developed for vessels with plaque. Such images were removed from the database, thus leading to a total of 200 images. The subjects' age ranged from 25 to 83 years (mean: 48.3 years; standard deviation: 9.9 years). Seventy subjects were male. All the patients were clinically evaluated before being included in the study and all the subjects signed an informed consent before the US examination. The study received the approval by the Institutional Committee of the Gradenigo Hospital .

### B. Automated Lumen Segmentation

The objective of this segmentation is to automatically segment the lumen in the carotid artery frame. The concept of automated lumen segmentation is based on finding the far adventitia ($AD_F$) border and reconstructing the Region of Interest (ROI) in which lumen lies. The ROI is then utilized to capture the lumen region. For automated $AD_F$ computation, we first remove the black frame surrounding the image [12]. This frame, which is a standard in all B-mode US images, interferes with the automated lumen segmentation system. We, therefore, cropped the images to maintain only the region containing the US data. This procedure was completely automated and relied on the data contained in the DICOM header of the images [12].

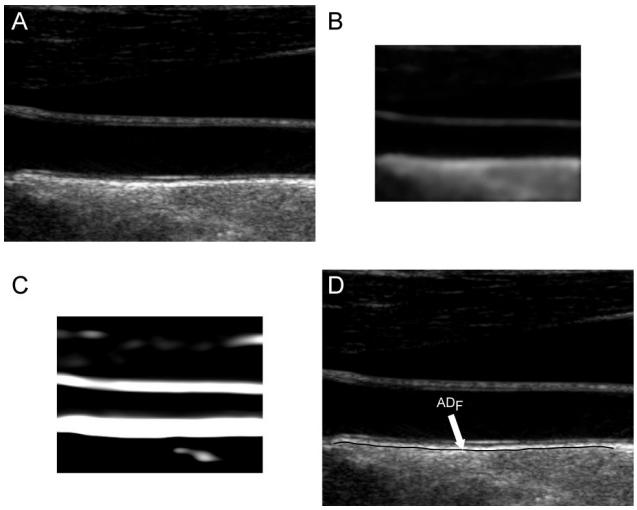


Fig. 1. (A) Original B-mode image. (B) Downsampled and despeckled image. (C) Convolution of image (B) with a first-order Gaussian kernel (D) Automated tracing of the far adventitia layer ($AD_F$) in image (A).

Subsequently, our procedure automatically recognizes the carotid artery in the image. We adopted a patented multi-resolution approach (CAMES [13] – a class of AtheroEdge™ systems from Global Biomedical Technologies, Inc., CA, USA), consisting of the following steps:

1. Downsampling: We downsampled the image (Fig. 1A) by a factor of 2 and attenuated the speckle noise (Fig. 1B). This process scaled the size of the carotid wall (nominally about 1 mm = about 16 pixels) to the optimal size of 8 pixels for the automated recognition.
2. Convolution with Higher Order Derivative: We filtered the image (Fig. 1B) by using a first-order derivative Gaussian filter (Fig. 1C). This filter is the equivalent of a high-pass filter, which enhances the representation of the objects having the same size of the kernel. Since we aimed at enhancing the representation of the carotid walls, we chose a kernel size of 8 pixels.
3. Heuristic Search for $AD_F$: Starting from the bottom of the image, the far carotid wall was recognized as it was a bright stripe of about 8 pixels size (Fig. 1D). As mentioned in step 1, the nominal value of the IMT is

about 1 mm which is equivalent to 8 pixels in the downsampled domain. Thus, the first-order Gaussian derivative kernel is size matched to the IMT and it outputs a white stripe of the same size as the far wall thickness. Our heuristic search considered the image column-wise. The intensity profile of each column was scanned from bottom to top (*i.e.,* from the deepest pixel moving upwards). The deepest region which had a width of at least 8 pixels was considered as the far wall.

4. Guidance Zone Creation: The output of this carotid recognition stage was the tracing of the far adventitia layer ($AD_F$) (a complete description of this procedure is given in [13]). We selected a Guidance Zone (GZ) in which we performed segmentation. The basic idea was to draw a GZ that comprised the far wall (*i.e.*, the intima, media, and adventitia layers) and the near wall. The average diameter of the carotid lumen is 6 mm, which roughly corresponded to 96 pixels at a pixel density of 16 pixels / mm. Therefore, we traced a GZ that had the same horizontal support of the $AD_F$ profile, and a vertical height of about 200 pixels. With this vertical size, which is double the normal size of the carotid, we ensured the presence of both artery walls in the GZ.
5. Lumen Segmentation: The lumen segmentation consists of a preprocessing step followed by a level set based segmentation method. The first preprocessing step is the inversion of the image *i.e.,* we subtract every pixel in the image from the maximum value of the image. We then multiply the image by a function of the gradient of the original image given by (1) below.

$$f(\nabla u) = \frac{1}{1+|\nabla u|} \quad (1)$$

Here $u$ indicates the image. The function is such that it takes low values (<<1) at the edges in the image and takes a maximum value of 1 in regions that are 'flat'. The lumen is then segmented using the active contour without edges algorithm or the Chan-Vese algorithm as described in [14] (Appendix A). The algorithm was chosen because of the piecewise constant nature of the cropped carotid artery images obtained from the previous step. The lumen, after preprocessing, is white and its grayscale intensity is high (>100) with noise. The walls of the artery that initially appear bright become dark (i.e. <50 grayscale intensity) after preprocessing. The Chan-Vese method is very effective for segmenting images made up of two piecewise constant regions which in our case correspond to the lumen and the carotid wall. The segmentation produces a binary image where the lumen is white (intensity of 1) and the wall intensity is 0. We would also like to point out that the algorithm is not influenced by the actual gray scale values in the carotid images giving us the flexibility to analyze images acquired with different settings. The algorithm is also robust to noise as it does not directly depend on the edges in the images. The pseudo-code for the entire automated segmentation algorithm is as follows:

A) Invert image *i.e.,* subtract image from maximum value in the image
B) Multiply with function given in (1)
C) Down sample image by a factor of 4. Since numerical Partial Differential Equations require long computing times, we down sampled the image to achieve convergence in a reasonable amount of time.
D) Initialize level set contour as a rectangle. The initial contour placement is automated. We computed a rectangular contour centered on the image.
E) Run the Chan-Vese algorithm for 1000 iterations. The number of iterations was arrived at by trial and error and it was sufficient for all test images across different databases.
F) Up sample the segmentation result, which is a binary image where the lumen is 1, to the original size of the image.
G) The presence of the jugular vein in some images causes the algorithm to segment both the carotid and the vein. In this case, employ a connected component analysis to determine which connected group is closer to the $AD_F$. The connected group closest to the $AD_F$ is taken as the carotid artery.
H) Apply morphological hole filling to remove holes in the binary segmentation result caused by the backscatter noise in the lumen.

### C. *Image Alignment for Composite Image Generation*

The first step in the automated IMT measurement algorithms like CALEX is the recognition of the Common Carotid Artery (CCA). For this purpose, the assumption by most of these feature-based algorithms is that the far wall of the CCA has the highest intensity in the image. To validate this assumption, it is necessary to locate the far wall and determine its intensity. If the ultrasound probe is exactly along the longitudinal axis of the CCA, the resulting image will show a nearly horizontal straight CCA with respect to the base edge of the image. However, not all CCA images are acquired parallel to the longitudinal axis. Sometimes, the probe can make a slight angle with the longitudinal axis of the CCA, and therefore, the resultant image will not have the CCA absolutely horizontal with respect to the base of the image. Such images will show a slightly titled CCA. In order to superimpose all these images to show that the cumulative far wall intensity is the highest, we register all CCA images with respect to an ideal image in which the CCA is parallel to the base edge. This is the main motivation for registering the images in our work.

A near straight artery image is used as a target image for all other images in the database. Lumen segmentations of binary images are affine transformed to estimate the rotation and translation of the floating image into the same orientation and position as target image. The free form deformation registration method using B-spline described in [15] was used for non-rigid registration. The method is a hierarchical transformation model where the local deformations are described by free form deformations modeled using B-splines.

Registration is performed by minimizing a cost function that is a combination of sum of squared differences and a cost function associated with the smoothness of the transformation. The free form deformation based on B-splines deforms the object by altering an underlying mesh of spline control points. The alteration produces smooth and continuous transformations. In two dimensions, we denote $x$ and $y$ as the coordinates of the image volume. Let $\varphi_{ij}$ denote the mesh of control points ($n_1$ x $n_2$). The deformations produced by the B-splines can be written as:

$$d(x,y,z) = \sum_{l=0}^{3}\sum_{m=0}^{3} B_l(u)B_j(v)\varphi_{i+l,j+m}$$
$$i = \left\lfloor \frac{x}{n_1} \right\rfloor - 1, \quad j = \left\lfloor \frac{y}{n_2} \right\rfloor - 1 \tag{2}$$

In (2), $B_l$ represents the basis functions of the B-splines, given by (3).

$$B_0(u) = \frac{(1-u)^3}{6}$$
$$B_1(u) = \frac{(3u^3 - 6u^2 + 4)}{6}$$
$$B_2(u) = \frac{(-3u^3 + 3u^2 + 3u + 1)}{6}$$
$$B_3(u) = \frac{u^3}{6} \tag{3}$$

The cost function for the registration is mathematically given as

$$C = \sum (I - T(F))^2 + \sum_x \sum_y \left[ \left( \frac{\partial^2 d}{\partial x^2} \right)^2 + \left( \frac{\partial^2 d}{\partial y^2} \right)^2 + . \right.$$
$$\left. 2\left( \frac{\partial^2 d}{\partial x \partial y} \right) \right] \tag{4}$$

Here, $I$ is the fixed target reference image, $F$ is the floating image transformed by $T$ (combined rigid and non-rigid transformation). The deformation $d$ is defined in (2) and the derivatives are with respect to spatial coordinates. In (4), the second term is the penalty term for smooth deformations and is the bending energy of a thin plate of metal. The optimization solves for the control point grid from which the deformations are calculated.

Non-rigid registration using B-splines based free form deformations is one of the popular methods for non-rigid registration of multi-modality images. The algorithm's main advantage compared to other methods is that it produces very smooth deformations due to B-splines and the transformed images are not overly distorted. Because of its use in multi-modality registration, information theoretic metrics are used as the cost function. For our application, we used the least squares criterion as we were registering 2D binary images oriented differently. It proved to be more effective than directly registering the grayscale carotid artery images. Several implementations of this algorithm are readily available in various languages. We used the Matlab implementation by Dr. Dirk-Jan Kroon available from Mathworks file exchange. The algorithm is generally slow (5 minutes per image pair). But in our case we are using it only for validation purposes and will not be a part of any commercial implementation. We also perform an initial affine registration that scales and aligns the floating image. The non-rigid registration is the final step to obtain a more accurate transformation field.

## III. Results

### A. Segmentation Results

The average distance between the manually traced Media-Adventitia (MA) boundary and the automatically traced $AD_F$ was 25.03 ± 19.47 pixels (1.54 ± 1.19 mm). This small distance indicates that the automatically traced $AD_F$ profile and the manually traced MA profile match, and therefore, the recognition of the carotid artery was successful. The segmented lumen of the fixed base carotid artery and a floating carotid artery image belonging to different patients are shown Fig. 2. The images are chosen to highlight the requirement for an affine transformation prior to a non-rigid registration.

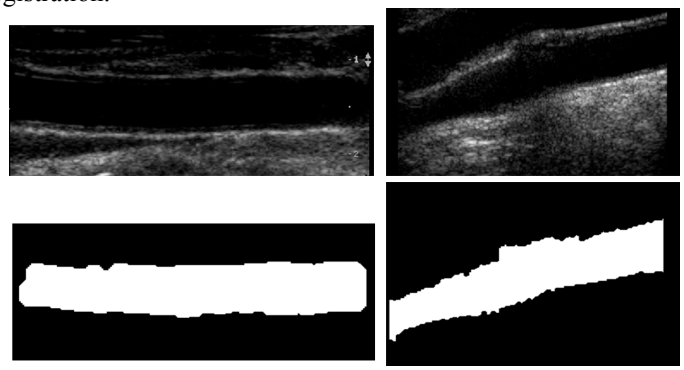

Fig. 2. Segmentation Results. Fixed reference image of carotid artery (Top left) and one of the 200 floating carotid artery images (Top right). Binary image of segmented fixed reference image lumen (Bottom left) and binary image of segmented floating image lumen (Bottom right).

### B. Registration Results

In Fig. 3, a typical registration result is shown. We have chosen two carotid artery images that were at an angle with respect to the horizontal. The transformation is the result of an affine transformation followed by the free form deformation. We chose a weighting factor of 0.01 for the smoothing term in the cost function. Typically, it took about 35 iterations for the affine registration to converge. Following affine, the non-rigid registration took 60 iterations to converge.

In Fig. 4, a surface plot of the sum of all registered images is shown. The grayscale sum image is also displayed. The window and level of the grayscale image are set to its minimum and maximum values. The results in Fig. 4 confirm our hypothesis qualitatively. To obtain quantitative evidence, we calculated the maximum value along every column in the sum image and confirmed that the maximum value along each column was from the far wall. In Fig. 5, the mean intensity and standard deviation from a 5x5 window centered on the same column along the near and far wall are shown. The far wall intensity is clearly higher and well separated from the average values along the near wall. A z-score was calculated by dividing the difference between the mean values of the corresponding 11 x 11 window along the far and near walls

and sum of their standard deviations. For all windows considered, the z-score was greater than 2.

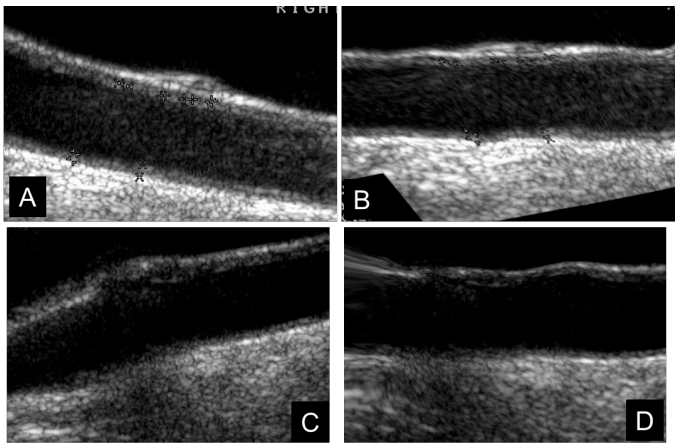


Fig. 3. Result of non-rigid free form deformation of two carotid artery images with the carotid artery at an angle with respect to the horizontal. (A) & (B) are the acquired and transformed image pairs of one carotid artery. Similarly (C) &(D) are acquired and transformed image pairs of the second carotid artery.

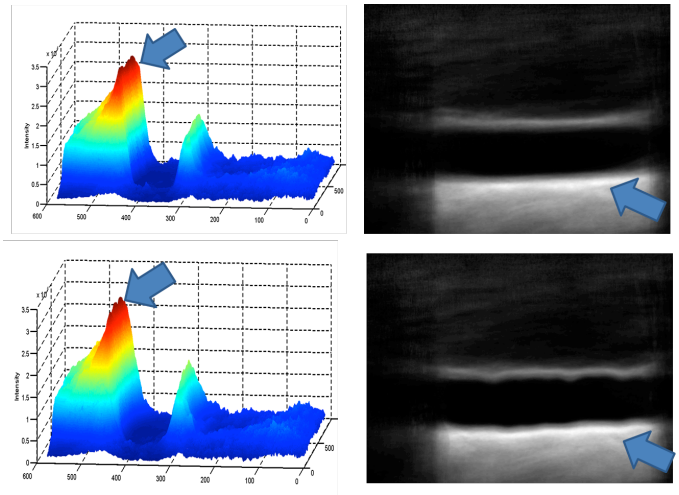

Fig. 4. Surface plot of the registered sum of 200 images showing intense far wall (Left). The same displayed as a 2D image (right). The top row image is the result of non-rigid registration while the bottom row image is the results using affine registration. The arrows point to the far wall.

## IV. DISCUSSION

In this work, we validated the hypothesis of far wall maximum brightness using a much larger dataset comprising of 200 images. Our approach was to register all the B-mode US images to a base fixed image which is considered carotid 'straight'. The US images of the carotid artery do not have many structures and there are no landmarks that can be used to assess the quality of registration. We used the intensity sum image to verify that the lumen volumes coincided. Since we used a non-rigid registration algorithm, we manually verified that the deformations are smooth and do not overly distort the carotid artery. Since the artery in different patients can be oriented at different angles and consequently be of different lengths in the image, we require an affine transformation to orient and scale the arteries appropriately. The non-rigid transformation aligns the edges of the segmented lumen. In many cases, non-rigid registration might not be required as the artery images are straight and do not have any distortions.

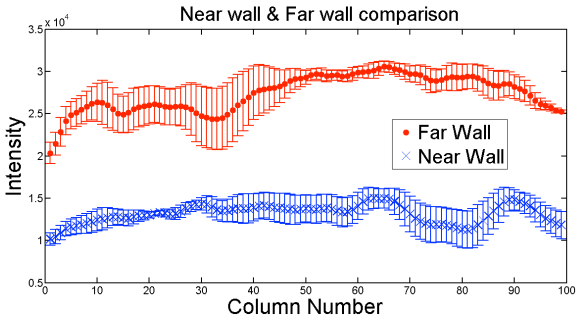


Fig. 5. Mean intensity and standard deviation along the far wall and near wall.

The registration accuracy in terms of sub-pixel metrics is not a hard requirement for this work. We wanted to verify that the far wall has higher intensity than the near wall in all images and for that purpose it is sufficient that the images be registered within the thickness of the far wall. Our hypothesis can be easily verified by visual inspection of Fig. 3 and Fig. 4 (3D plots). In Fig. 4, it can be seen that the far wall has a relatively higher intensity compared to that of the near wall. Quantitative results are depicted in Fig. 5, and the z-score of greater than 2 also verifies our hypothesis.

The automated $AD_F$ detection method proved very robust and had a 100% success rate. This ensured the possibility of an accurate segmentation, which is based on $AD_F$ tracing. The major merits of this automated adventitia recognition is that the multiresolution stage is strictly linked to the pixel density of the image. This gave robustness to the method, as in the multiresolution framework, we always worked with a Gaussian kernel size equal to the expected IMT value.

The binary lumen image has a jagged appearance. The binary image edges can be smoothed to obtain a continuous line edge but the impact on the registration is not significant. We are using the lumen binary images to estimate affine transforms and correct for orientation and scaling. The final non-rigid transformation makes small changes to arteries that are bent or slightly curved and aligns them with the straight fixed image. Small errors in segmentation do not impact the affine transformation in terms of orientation angle and scaling. Also, any significant curve in the arteries would be adjusted by the non-rigid transform despite the presence of these jagged edges.

The segmentation and subsequent registration of the binary image of the lumen can be further improved by increasing the Dynamic Range (DR) of the acquisition [16]. Increasing DR improves the contrast and reduces the variance of the image producing sharply peaked histograms of carotid US images. Increased contrast and variance improve the segmentation as it is based on the assumption that the image is made up of regions of constant intensity.

We also evaluated affine registration on our data sets. Although the non-rigid registration provides a more accurate registration, an affine registration scheme is sufficient for

alignment of the lumen. The lumen edges can be smoothed to remove the kinks or jaggedness prior to registration. For the purposes of this paper, we conclude that affine registration would be sufficient**.**

## V. CCA Recognition and IMT Measurement

The brightness of the far wall is exploited by the CALEX 3.0 system to measure IMT. CALEX 3.0 is the latest release of an integrated approach combining feature extraction, fitting, and fuzzy classification we developed in 2010 [9, 17]. In Fig. 6, we show a typical carotid artery and the result of the adventitia localization by our system, CALEX 3.0. In this work, we acquired longitudinal images wherein the ultrasound probe head is held along the axis of the CCA. Therefore, even if the probe head is slightly titled away from the longitudinal axis of the CCA, the angle of acquisition has a very subtle change and the resulting tilt in the carotid artery will only be minor. This subtle change/tilt is compensated by the registration algorithm described earlier, and therefore, the carotid shape does not influence the algorithm. Measuring IMT involves automatic identification and segmentation of the carotid artery lumen and localizing the MA boundary and the Lumen-Intima (LI) boundary. In this section, we present the steps involved in these processes, and the resultant IMT values.

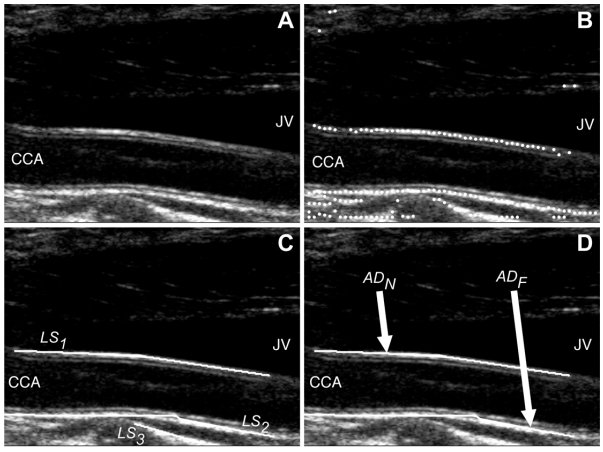


Fig. 6. CALEX process for Adventitia localization. US image of carotid artery (A). Automatic selection of seed points based on higher intensity of far wall (B). Rejection of seed points not belonging to adventitia and connecting seed points to obtain line segments (C). Identification of far and near Adventitia (D).

### *A. Automated carotid localization/recognition*

Despite the use of a validation procedure, previous version of CALEX 1.0 could still inaccurately trace the far adventitia. In Fig. 6, we show how the far wall adventitia is localized. Initial seed points are chosen based on local maxima, which are assumed to be in the far wall. We have validated this assumption by registering an entire database of images. For selecting the true seed points, we used a linear discriminator that bins the true seed points and false-negative seed points separately. The objective is to find the possible seed points that are above a certain threshold $u_T$ and are likely to be the edges of the lumen but not inside the lumen. To distinguish true seed points from local maxima due to background noise, we used a linear discriminator **v** applied to the vector of seed candidates with the property vector **p** made up of *Intensity*, *e*, (which corresponds to the height of the seed candidate on the vertical intensity profile) and *Breadth*, *b*, (which corresponds to the distance between the two neighbouring local minima that are on the opposite sides of the seed candidate). Now, the criteria for seed point selection were based on the threshold $u_T$, mathematically laid out to follow the equality: $\mathbf{p} \cdot \mathbf{v} > u_T$ (here, $\cdot$ denotes the dot product between two vectors). Here, $u_T$ is equal to 0 [8]. The existing points were then connected according to their proximity and orientation and classified as near and far wall of the adventitia [8].

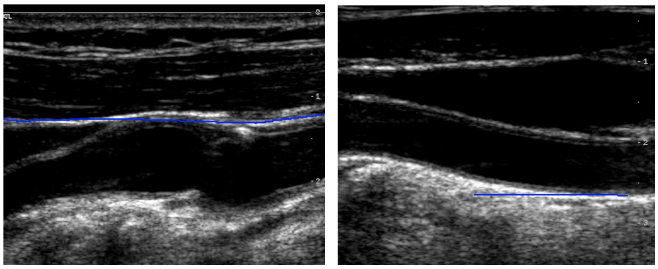

Fig. 7. Typical far-wall identification errors of the former version CALEX 1.0.

CALEX 3.0 incorporates a robust algorithm to avoid the Jugular Vein (JV) and to avoid incorrect tracings of the $AD_F$. As depicted in Fig. 7, the typical far-wall identification errors of CALEX 1.0 are:

(1) Selected line segments are along the JV above common carotid artery.

(2) The whole (or part) of selected line segments deviates from the adventitia layer of the far wall of CCA.

The first error can be fixed by observing that when the line segment is traced on the JV instead of the $AD_F$, its upper side is brighter than its lower side, while it should be the opposite. Based on this observation, we introduce a new feature, called *isadf*, for each valid line segment. Conceptually, the higher the value of the *isdaf* of a line segment, the higher the probability that line segment corresponds to the far adventitia. For each valid line segment, the *isadf* feature is calculated as:

$$isadf = \frac{\sum_{i=0}^{N}\sum_{j=0}^{M} I(x_i, y_i + j)}{\sum_{i=0}^{N}\sum_{j=0}^{M} I(x_i, y_i - j)} \tag{5}$$

In (5), $N$ is the number of points on the line segment, $M$ (= 30 pixels) is the sample distance, and $I$ is the input image. When the *isdaf* value of a given line segment is lower than 1, it means that the upper side of that segment is brighter than the lower side. Therefore, it cannot be the adventitia layer (which we proved to be the brightest image feature) and should be discarded.

The second error is fixed by a refinement procedure. For each point $p$ on the detected far-wall adventitia, we extract the column-wise signal as given by (6):

$$s = f(I(x, y+i)), D_{lower} < i < D_{upper} \tag{6}$$

where $D_{upper}$ (=50) is upper sample limit, and $D_{lower}$ (=-5) is lower sample limit. Then, we find the nearest local maxima (or minimum) point $q$ such that the absolute intensity difference between point $p$ and $q$ is larger than a predefined

threshold $I_T$; otherwise point $p$ is discarded.

Fig. 8 shows the original and initial CALEX 1.0 $AD_F$ profile (*left panel*) and the refinement made by CALEX 3.0 (*right panel*).

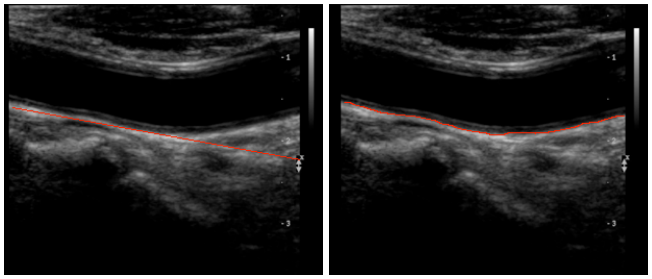

Fig. 8. Left panel: Detection of the $AD_F$ by CALEX 1.0. Right panel: Refined and optimized $AD_F$ profile detected by CALEX 3.0.

### B. Far wall segmentation

Once the near and far adventitia layers are automatically traced, a guidance zone (GZ) is delineated based on the far adventitia profile ($AD_F$). The GZ has same horizontal length of the $AD_F$ profile and a height equal to 30 pixels. We determined this specific value of 30 pixels after an extensive benchmark on our image dataset. Since the pixel dimension was 0.0625 mm in both the vertical and horizontal direction, and since the average IMT is about 1mm (*i.e.*, 16 pixels), we took a GZ vertical size that was double the average IMT. Therefore, we made sure that we included the entire distal wall and a portion of the carotid lumen.

CALEX 3.0 was then used to classify the pixels into the GZ. We input the intensity profile of each column of the image into a fuzzy *K-means* classifier. We fixed the number of classes equal to three: i) the carotid wall (made of dark pixels); ii) the intima and media layers (made of pixels with an average gray level), and iii) the adventitia layer (made of bright pixels). The transition point between class i) and class ii) was the LI interface, whereas the transition between classes ii) and iii) was the MA interface. The IMT value was computed as distance between the LI and MA profiles for each image.

Fig. 9 shows samples of automated CALEX 3.0 segmentation of the far carotid wall and LI/MA tracings. To show the robustness of the method and the validity of our registration hypothesis in all the possible conditions, we have reported in Fig. 9 the CALEX 3.0 segmentations for different carotid morphologies.

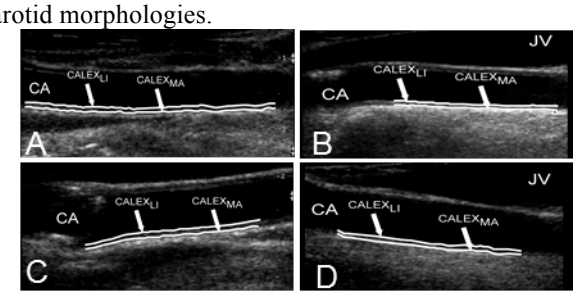


Fig. 9. Samples of CALEX 3.0 automated segmentation for different carotid morphologies, showing the robustness of the technique. A) Straight and horizontally placed carotid. B) Curved carotid with jugular vein overlapped (JV). C) Inclined carotid with positive slope. D) Inclined carotid with negative slope. ($CALEX_{LI}$ – CALEX lumen-intima boundary; $CALEX_{MA}$ – CALEX media-adventitia boundary).

### C. Distance and performance metric

We adopted the Polyline Distance Metric (PDM) to compute the IMT value from the LI/MA profiles. This metric was proposed by Suri *et al.* [18] and used in cardiological studies. The PDM is an optimal distance metric to compute the distance between boundaries given by vertices, because it is almost insensitive to the number of points constituting the boundaries. For each vertex $i$ belonging to LI, the minimum distance from the line segments of MA is computed. Let this distance be $d_{i\text{-}MA}$. Then, the overall distance between vertices of LI and the segments of MA is computed as in (7):

$$d_{LI-MA} = \sum_{i=1}^{N_{LI}} d_{i-MA} \tag{7}$$

where $N_{LI}$ is the number of vertices of the LI boundary. Similarly, the distance $d_{MA\text{-}LI}$ is computed, which is the overall distance of the vertices of MA from the segments of LI. The PDM is defined as:

$$PDM_{LI,MA} = \frac{d_{LI-MA} + d_{MA-LI}}{N_{LI} + N_{MA}} \tag{8}$$

In (8), $N_{MA}$ is the number of vertices of the MA profile. The IMT by CALEX 3.0 and the reference IMT ($IMT_{GT}$) were computed as:

$$\begin{aligned} IMT_{CALEX} &= PDM_{CALEX_{LI},CALEX_{MA}} \\ IMT_{GT} &= PDM_{GT_{LI},GT_{MA}} \end{aligned} \tag{9}$$

In (9), GT is relative to manually traced profiles which we considered as Ground Truth. The IMT value was measured for each image and the overall system performance was computed in terms of IMT measurement bias, absolute error, and squared error compared to $IMT_{GT}$.

### D. IMT measurement performance

Table I reports the overall system performance of CALEX 3.0 compared to GT. To completely characterize the system performance, we compared the IMT measurements by CALEX 3.0 to the manual measurements (GT). The results are given as mean value ± standard deviation on the 200 images database. We computed the IMT measurement bias $\varepsilon$, the absolute error $\delta$ and the squared error $\varepsilon^2$ defined as:

$$\begin{aligned} \varepsilon &= \frac{1}{N}\sum_{i=1}^{N}\left(IMT^i{}_{CALEX} - IMT^i{}_{GT}\right) \\ \delta &= \frac{1}{N}\sum_{i=1}^{N}\left|IMT^i{}_{CALEX} - IMT^i{}_{GT}\right| \\ \varepsilon^2 &= \frac{1}{N}\sum_{i=1}^{N}\left(IMT^i{}_{CALEX} - IMT^i{}_{GT}\right)^2 \end{aligned} \tag{10}$$

where $N$ is the number of the images in the testing database, $IMT^i{}_{CALEX}$ is the IMT measurement by CALEX 3.0 relative to the *i-th* image, and $IMT^i{}_{GT}$ is the ground-truth IMT measurement of the *i-th* image. The IMT bias was equal to –0.029±0.228 mm, the IMT absolute error to 0.144±0.179 mm,

and the IMT squared error to 0.052±0.151 mm$^2$. The IMT estimated by CALEX 3.0 on the dataset was 0.836±0.206 mm, which is very close to the ground-truth of 0.864±0.221 mm.

We also defined the Figure-of-Merit (FoM) for CALEX 3.0, which was defined as:

$$FoM = 100 - \left| \frac{\overline{IMT}_{CALEX} - \overline{IMT}_{GT}}{\overline{IMT}_{GT}} \right| \cdot 100 \qquad (11)$$

where $\overline{IMT}_{GT}$ was the average IMT value by GT, and $\overline{IMT}_{CALEX}$ the average IMT value by CALEX 3.0 (*i.e.,* these two values are those reported in the first row of Table I). The FoM was equal to 96.7%. Fig. 10A reports the Bland-Altmann plot for the CALEX 3.0 and GT estimates of the IMT. It can be shown that CALEX 3.0 has a much reduced bias (equal to 0.029 mm, which means about 3% of bias with respect to a nominal IMT value of 1 mm). Moreover, the reproducibility of CALEX 3.0 is good, because the standard deviation of the IMT error is 0.206 mm. Previous studies documented that the reproducibility of the IMT measurements made by expert sonographers can as low as 0.15 mm [1]. Fig. 10B shows the distribution of the IMT bias. The black line represents the cumulative function.

TABLE I – OVERALL SYSTEM PERFORMANCE OF CALEX 3.0 COMPARED TO GROUND TRUTH

| | CALEX 3.0 | Ground Truth |
|---|---|---|
| IMT value (mm) | 0.836±0.206 | 0.864±0.221 |
| IMT bias (mm) | -0.029±0.228 | |
| IMT absolute error (mm) | 0.144±0.179 | |
| IMT squared error (mm$^2$) | 0.052±0.151 | |

From a clinical point of view, the Bland-Altmann is the most important representation of the performance of a technique. The accuracy of the technique (*i.e.*, the IMT bias) was less than 3% of the nominal IMT value. In this regard, a bias of 30 μm is clinically acceptable. The reproducibility of the IMT measurement (*i.e.*, the standard deviation of the IMT bias, which determines the width of the dashed lines in the Bland-Altmann plot) is a scope of improvement. Currently, the most accurate IMT measurement techniques are user-driven. When an expert operator drives and corrects the segmentation, the IMT bias can be reduced to 0.01±0.02 mm [19]. Automated techniques usually have a reproducibility that is between five and ten times worse [8,10,17]. Our team is now working specifically to increase the reproducibility of automated IMT measurement strategies.

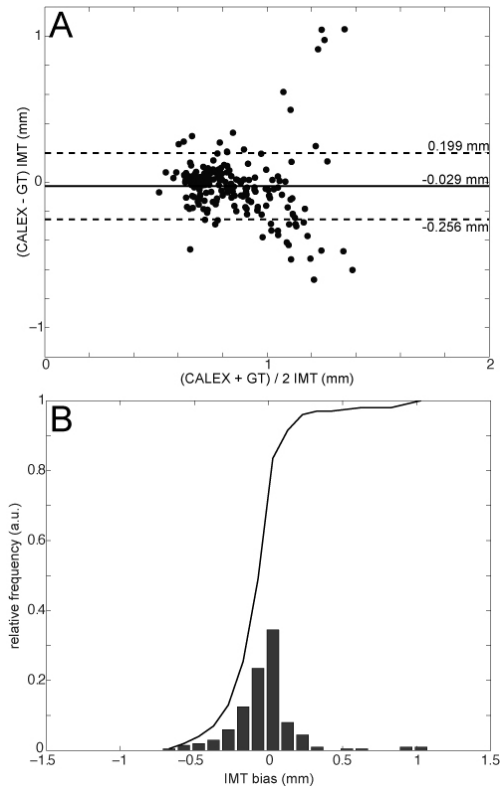


Fig. 10. Characterization of the CALEX 3.0 IMT performance. A) Bland-Altmann plot of the CALEX 3.0 and GT IMT values. B) Histogram distribution of the IMT measurement bias. The black line represents the cumulative function.

## VI. CONCLUSION

The far wall appears bright in a typical US carotid artery image. We have exploited this feature for automatic IMT measurement in our CAD software (a class of AtheroEdge® system from Global Biomedical Technologies, Inc., CA, USA). In this work, we validated the hypothesis that the far wall is bright compared to the near wall by taking into consideration a US database of 200 images. In the process, we have also put together a scheme for carotid artery segmentation and registration in follow-up US studies. Since we were able to register our database of images successfully we believe that this system can be used for registering multiple studies corresponding to the same patient. We have used a novel and completely automated segmentation algorithm based on level sets. We also applied our IMT measurement system (CALEX) and showed its error of about 30 μm. This system will be useful not only as a standalone technique but also as part of more complex systems as described in [20] that can improve image data retrieval, storage and diagnosis.

## REFERENCES

[1] P. J. Touboul, M. G. Hennerici, S. Meairs et al., "Mannheim carotid intima-media thickness consensus (2004-2006). An update on behalf of the Advisory Board of the 3rd and 4th Watching the Risk Symposium, 13th and 15th European Stroke Conferences, Mannheim, Germany, 2004, and Brussels, Belgium, 2006," *Cerebrovasc Dis*, vol. 23, no. 1, pp. 75-80, 2007.

[2] I. M. van der Meer, M. L. Bots, A. Hofman, A. I. del Sol, D. A. van der Kuip, and J. C. Witteman, "Predictive value of noninvasive measures of

atherosclerosis for incident myocardial infarction: the Rotterdam Study," *Circulation,* vol. 109, no. 9, pp. 1089-94, Mar. 2004.
[3] P. Poredos, "Intima-media thickness: indicator of cardiovascular risk and measure of the extent of atherosclerosis," *Vasc Med,* vol. 9, no. 1, pp. 46-54, Feb. 2004.
[4] K. Nasu, E. Tsuchikane, O. Katoh, N. Tanaka, M. Kimura, M. Ehara, Y. Kinoshita, T. Matsubara, H. Matsuo, K. Asakura, Y. Asakura, M. Terashima, T. Takayama, J. Honye, A. Hirayama, S. Saito, and T. Suzuki, "Effect of fluvastatin on progression of coronary atherosclerotic plaque evaluated by virtual histology intravascular ultrasound," *JACC Cardiovasc Interv,* vol. 2, no. 7, pp. 689-96, Jul. 2009.
[5] C. Liguori, A. Paolillo, and A. Pietrosanto, "An automatic measurement system for the evaluation of carotid intima–media thickness," *IEEE Trans .Instrum. Meas.*, vol. 50, no. 6, pp. 1684–1691, Dec. 2001.
[6] D. Cheng, A. Schmidt-Trucksass, K. Cheng, and H. Burkhardt, "Using snakes to detect the intimal and adventitial layers of the common carotid artery wall in sonographic images," *Comput. Methods Programs Biomed.*, vol. 67, no. 1, pp. 27–37, Jan. 2002.
[7] M. A. Gutierrez, P.E. Pilon, S. G. Lage, L. Kopel, R. T. Carvalho, and S. S. Furuie, "Automatic measurement of carotid diameter and wall thickness in ultrasound images," in *Proc. Comput. Cardiol.*, 2002, vol. 29, pp. 359–362
[8] F. Molinari, G. Zeng, J. S. Suri, "An integrated approach to computer-based automated tracing and its validation for 200 common carotid arterial wall images," *J. Ultrasound Med.*, vol. 29, no. 3, pp. 399-418, 2010.
[9] S. Delsanto, F. Molinari, P. Giustetto, W. Liboni, S. Badalamenti, and J. S. Suri, "Characterization of a completely user-independent algorithm for carotid artery segmentation in 2-D ultrasound images," *IEEE Trans. Instrum. Meas.,* vol. 56, no. 4, pp. 1265-1274, 2007.
[10] F. Molinari, U. Rajendra Acharya, G. Zeng, K. M. Meiburger, and J. S. Suri, "Completely automated robust edge snapper for carotid ultrasound IMT measurement on a multi-institutional database of 300 images," *Med. Biol. Eng. Comput.*, Apr 21, (in press).
[11] J. S. Suri, Y. Guo, R. Janer, "Entropy-Based Vs. Spline-Based Registration Techniques for X-ray Phantom Mammograms produced by Fischer's Full Field Digital Mammography and Ultrasound System (FFDMUS): Combined Segmentation and Registration Framework" *IASTED*, BioMed, 2005.
[12] F. Molinari, W. Liboni, P. Giustetto, S. Badalamenti, and J. S. Suri, "Automatic computer-based tracings (ACT) in longitudinal 2-D ultrasound images using different scanners," *J. Mech. Med. Biol.,* vol. 9, no. 4, pp. 481-505, 2009.
[13] F. Molinari, C. Pattichis, G. Zeng, L. Saba, Rajendra Acharya U., R. Sanfilippo, A. Nicolaides, and J. S. Suri, "Completely Automated Multi-resolution Edge Snapper (CAMES) – A New Technique for an Accurate Carotid Ultrasound IMT Measurement: Clinical Validation and Benchmarking on a Multi-Institutional Database," *IEEE Trans. Image Process.*, 2011 (accepted).
[14] T. F. Chan, and L. A. Vese, "Active contours without edges," *IEEE TRANS. Image Proc.*, vol. 10, no. 2, pp. 266-277, Feb. 2001.
[15] D. Rueckert, L. I. Sonoda, C. Hayes, D. L. G. Hill, M. O. Leach, and D. J. Hawkes, "Nonrigid registration using free-form deformations: Application to breast MR images," *IEEE Trans. Med. Imaging*, vol. 18, no. 8, pp. 712-721, Aug. 1999.
[16] S. Golemati, J. S. Stoitsis, D. A. Perakis, E. Varela, A. Alexandridi, C. H. Davos, and K. S. Nikita, "Carotid artery motion estimation from sequences of B-mode ultrasound images: Effect of scanner settings and image normalization," *IEEE Trans. Instrum. Meas.,* vol. 58, no. 7, pp. 2102-2112, 2009.
[17] F. Molinari, G. Zeng, and J. S. Suri, "Intima-media thickness: setting a standard for completely automated method for ultrasound," *IEEE Trans. Ultrason., Ferroelectr., Freq. Control*, vol. 57, no. 5, pp. 1112-1124, 2010.
[18] J. S. Suri, R. M. Haralick, and F. H. Sheehan, "Greedy algorithm for error correction in automatically produced boundaries from low contrast ventriculograms," *Pattern Anal. Appl.*, vol. 3, no. 1, pp. 39-60, 2000.
[19] F. Faita, V. Gemignani, E. Bianchini, C. Giannarelli, L. Ghiadoni, M. Demi, "Real-time measurement system for evaluation of the carotid intima-media thickness with a robust edge operator," *J. Ultrasound Med.*vol. 27, no. 9, pp. 1353-1361, Sep. 2008.
[20] S. G. Mougiakakou, I. K. Valavanis, N. A. Mouravliansky, K. S. Nikita, A. Nikita, "DIAGNOSIS: A Telematics-Enabled system for medical image archiving, management, and diagnosis assistance", *IEEE Trans. Instrum. Meas*, vol. 58, no. 7, Jul. 2009.

## APPENDIX

Following the description in [14], we formulate the segmentation problem as an energy minimization problem to find the optimum curve segmenting the regions. The energy term to be minimized can be written as

$$E = \int_{cin} |u_0 - c_1|^2 dxdy + \int_{cout} |u_0 - c_2|^2 dxdy \quad (12)$$

where $c_{in}$ and $c_{out}$ refer to the regions enclosed by the optimum curve $C$ that separates the two regions in the image $u_0$. The terms $c_1$ and $c_2$ are the average values of the two regions. We can also add regularization terms that are proportional to the length of the curve ($L_c$) and the area of the curve ($A_c$).

$$\lambda_1 \int_{cin} |u_0 - c_1|^2 dxdy + \lambda_2 \int_{cout} |u_0 - c_2|^2 dxdy + \nu A_c + \mu . L_c \quad (13)$$

Here, $\mu$, $\nu$, $\lambda_1$ and $\lambda_2$ are fixed parameters. The level set formulation is obtained by replacing the curve $C$ with a level set function $\phi$ such that $C$ is the level set with value 0. The function $\phi$ takes values less than zero inside the contour and positive values outside the contour. The energy is rewritten as

$$\begin{aligned} &\lambda_1 \int_{\Omega} |u_0 - c_1|^2 H_\varepsilon(\phi(x,y)) dxdy + \\ &\lambda_2 \int_{\Omega} |u_0 - c_2|^2 (1 - H_\varepsilon(\phi(x,y)) dxdy + \\ &+ \mu \int_{\Omega} \delta_\varepsilon |\nabla \phi(x,y)| dxdy \end{aligned} \quad (14)$$

where $H_\varepsilon$ is the regularized version of the Heaviside function given by (15).

$$\begin{aligned} &H_\varepsilon(z) = 1, z > \varepsilon \\ &H_\varepsilon(z) = 0, z < -\varepsilon \\ &H_\varepsilon(z) = \frac{1}{2}\left[1 + \frac{z}{\varepsilon} + \frac{1}{\pi}\sin\left(\frac{\pi z}{\varepsilon}\right)\right], |z| \le \varepsilon \end{aligned} \quad (15)$$

We used a value of 10e-5 for $\varepsilon$. The Heaviside function is defined as 1 if its argument is non-negative and 0 otherwise. The derivative of the Heaviside function is the delta function ($\delta_\varepsilon$). $\Omega$ is the domain of the level set function. The associated Euler-Lagrange equation for $\phi$ is given by (16) below

$$\frac{\partial \phi}{\partial t} = \delta_\varepsilon(\phi) \begin{bmatrix} \mu . div\left(\frac{\nabla \phi}{|\nabla \phi|}\right) - \lambda_1 . (u_0 - c_1)^2 + \\ \lambda_2 . (u_0 - c_2)^2 \end{bmatrix} \quad (16)$$

The boundary conditions are

$$\begin{aligned} &\frac{\delta_\varepsilon(\phi)}{|\Delta \phi|} \frac{\partial \phi}{\partial \vec{n}} = 0, \partial \Omega \\ &\phi(0,x,y) = \phi_0(x,y) \end{aligned} \quad (17)$$

The equation is discretized and solved numerically.

**Filippo Molinari**, **PhD,** was born in Piacenza, Italy. He received the Italian Laurea degree and the Ph.D. in Electronics from the Politecnico di Torino, Torino, Italy, in 1997 and 2000, respectively. Since 2002, he is Assistant Professor on faculty of the Dept. of Electronics of the Politecnico di Torino. His research topics include the analysis of biosignals and the biomedical image processing applied to the computer-aided diagnosis and therapy. In the field of ultrasound imaging, Dr. Molinari developed diagnosis procedure for vascular applications and thyroid assessment. Dr. Molinari is member of the IEEE Engineering in Medicine and Biology Society (EMBS), of the Italian

Group of Bioengineering (GNB), and of the American Institute for Ultrasound in Medicine (AIUM).

**U Rajendra Acharya, PhD, DEng** is a Visiting faculty in Ngee Ann Polytechnic, Singapore, Adjunct faculty in Singapore Institute of Technology- University of Glasgow degree programme, Singapore, Associate faculty in SIM University, Singapore and Adjunct faculty in Manipal Institute of Technology, Manipal, India. He received his Ph.D. from National Institute of Technology Karnataka, Surathkal, India and D Engg from Chiba University, Japan. He has published more than 220 papers, in refereed international journals (122), international conference proceedings (40), book chapters (62), books (11 including in Press) with h-index of 14. He has worked on various funded projects with grants worth more than 1.5 million SGD. He is in the editorial board of many journals and served as Guest Editor for many journals. His major interests are in Biomedical Signal Processing, Bio-imaging, Data mining, Visualization and Biophysics for better healthcare design, delivery and therapy.

**S Vinitha Sree, PhD,** is a visiting scientist at the Global Biomedical Technologies Inc., CA, USA. She received her Masters in Biomedical Engineering and her PhD from Nanyang Technological University, Singapore. Her areas of interest include medical data mining, breast imaging systems, and healthcare systems and management. She has published over 26 peer-reviewed publications, and is an associate editor for JMIHI and a reviewer for JMMB.

**Ganapathy Krishnamurthi PhD** is currently working in the CT Clinical Innovation Center at Mayo Clinic. He received his MS in Physics (2001) and PhD in Medical Physics (2008) from Purdue University. His research interests include Biomedical image processing, Bio-imaging and functional imaging using CT.

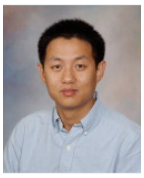

**Guang Zeng, PhD,** received the B.S. degree from Xiangtan University, China in 1998. He received the M.S. degree in 2005 and the Ph.D. degree in 2008 from Clemson University, SC, USA, both in Electrical Engineering. He is currently working in the Aging and Dementia Imaging Research Laboratory, Mayo Clinic, Rochester, MN. His research interests include biomedical image processing, pattern recognition and computer vision.

**Luca Saba, MD,** received the MD degree from the University of Cagliari, Italy in 2002. Today he works in the A.O.U. of Cagliari. Dr Saba research fields are focused on Neuroradiology, Multi-Detector-Row Computed Tomography, Magnetic Resonance, Ultrasound, and Diagnostic in Vascular Sciences.
His works, as lead author, achieved more than **75** high impact factor, peer-reviewed, Journals. Dr. Saba has written 7 book chapters and he presented more than 400 papers in National and International Congress. Dr Saba is member of the Italian Society of Radiology (SIRM), European Society of Radiology (ESR), Radiological Society of North America (RSNA), American Roentgen Ray Society (ARRS) and European Society of Neuroradiology (ESNR).

**Andrew Nicolaides, MS, FRCS, PhD (Hon)** graduated from Guy's Hospital Medical School, London University, London, U.K., in 1962. He received the M.S. degree from the Royal College of Surgeons of England, London, U.K., and the F.R.C.S., and F.R.C.S.E. degrees from the Royal College of Surgeons of England, London, and the Royal College of Surgeons of Edinburgh, Midlothian, U.K., in 1967. He is currently the Professor Emeritus at Imperial College, London and an Examiner for M.S. and Ph.D. degrees for London University, London. He is also a "Special Scientist" at the University of Cyprus, Nicosia, Cyprus, and theMedical Director of theVascular Screening and Diagnostic Centre, London. His current research interests include the genetic risk factors for cardiovascular disease, identification of individuals at risk and the development of effective methods of prevention, especially stroke. He is Editor-in-Chief of International Angiology and is on the Editorial Board of many vascular journals. He is the coauthor of more than 500 original papers and editor of 14 books.

**Jasjit S. Suri, PhD, MBA, Fellow AIMBE,** is an innovator, visionary, scientist, and an internationally known world leader, has spent over **25** years in the field of biomedical engineering/sciences and its management. Dr. Suri has written over **350** peer-reviewed technical publications. He has championed the field imaging sciences. He received his Masters from University of Illinois, Chicago, Doctorate from University of Washington, Seattle, and Executive Management from Weatherhead School of Management, CWRU, Cleveland. Dr. Suri is a committee member of several journals and companies. Dr. Suri was crowned with President's Gold medal in 1980 and the *Fellow of American Institute of Medical and Biological Engineering* (AIMBE), awarded by National Academy of Sciences, Washington DC in 2004. Dr. Suri has been the chairman of IEEE Denver section and has won over 50 awards during his career.